Volume 15, Issue 3, 152526 (1-13)

Iranian Journal of Catalysis (IJC)

https://doi.org/10.57647/j.ijc.2025.1503.26

Photoreduction deposition and characterization of heterostructure Pt/ZnO nanocomposites used for UV-light-driven photocatalysis

Anukorn Phuruangrat[1,*], Yothin Chimupala[2], Asanee Somdee[3], Budsabong Kuntalue[4], Titipun Thongtem[5,6], Somchai Thongtem[5,7,*]

[1]*Division of Physical Science, Faculty of Science, Prince of Songkla University, Hat Yai, Songkhla 90112, Thailand.*
[2]*Department of Industrial Chemistry, Faculty of Science, Chiang Mai University, Chiang Mai 50200, Thailand.*
[3]*Faculty of Science, Energy and Environment, King Mongkut's University of Technology North Bangkok, Rayong Campus, Rayong 21120, Thailand.*
[4]*Advanced Scientific Instruments Unit, Faculty of Science, Chiang Mai University, Chiang Mai 50200, Thailand.*
[5]*Materials Science Research Center, Faculty of Science, Chiang Mai University, Chiang Mai 50200, Thailand.*
[6]*Department of Chemistry, Faculty of Science, Chiang Mai University, Chiang Mai 50200, Thailand.*
[7]*Department of Physics and Materials Science, Faculty of Science, Chiang Mai University, Chiang Mai 50200, Thailand.*

[*]**Corresponding authors:** phuruangrat@hotmail.com, schthongtem@yahoo.com

Original Research

Received:
27 January 2025
Revised:
21 April 2025
Accepted:
5 May 2025
Published online:
13 May 2025
Published in issue:
30 September 2025

© 2025 The Author(s). Published by the OICC Press under the terms of the Creative Commons Attribution License, which permits use, distribution and reproduction in any medium, provided the original work is properly cited.

Abstract:

0.5%, 1.0%, and 3.0% Pt/ZnO nanocomposites synthesized by the photoreduction deposition method were used for studying UV-light-driven photodegradation of methylene blue (MB). Phase and composition of heterostructure 3.0% Pt/ZnO nanocomposites were indexed to a hexagonal ZnO phase doped with face-centered cubic (FCC) Pt structure characterized by XRD. According to FTIR and Raman analyses of Pt/ZnO nanocomposites, the vibration of ZnO was influenced by the strong interaction of metallic Pt nanoparticles. SEM images of heterostructure Pt/ZnO nanocomposites show that they were composed of flower-like ZnO structures with spherical Pt nanoparticles decorated on the surface of nanoplate petals. The photocatalytic performance of the as-prepared samples was evaluated by deleting methylene blue (MB) as a toxic dye model under UV light irradiation. The loaded Pt nanoparticles played the role in preventing the recombination of photo-excited electrons and photo-induced holes and enhancing the photocatalytic reaction of ZnO. In this research, 0.5% Pt/ZnO nanocomposites were the best UV-light-driven photocatalyst with % degradation efficiency of 97.37% within 180 min and with $^{\bullet}O_2^-$ and h^+ as main active species.

Keywords: Main active radicals; Pt/ZnO nanocomposites; Scavenger agents; UV-light-driven photocatalyst

1. Introduction

In recent years, azo organic pollutants drained out of the paper, pharmaceutical, textile, and dyeing industries have had a very great impact on the environment and living organisms [1–4]. Among azo organic dyes, methylene blue ($C_{16}H_{18}ClN_3S$, MB) is an aromatic heterocyclic basic dye with highly water-soluble properties, and a stable solution begins to exist at room temperature [5, 6]. It is a commercial dye used in textile industries and is drained into natural sources. It is harmful to human health, such as respiratory distress, abdominal disorder, blindness, digestive system, mental disorder, and destructive effect on the environment because of its toxic, carcinogenic, and non-biodegradable properties [5–7]. Advanced and effective treatment of photocatalytic semiconductors plays the role in absorbing photonic energy and generating excited electrons in the conduction band (CB) and inducing holes in the valence band (VB). In the end, azo organic dye molecules present in wastewater are degraded by direct and indirect pathways [8–10]. In the

direct photocatalytic pathway, the electron-hole pairs can directly attack the adsorbed pollutant on the surface of the semiconductor photocatalyst [8, 9]. For the indirect photocatalytic pathway, the electrons and holes react with O_2 and H_2O/OH^- to produce $^{\bullet}O_2^-$ and $^{\bullet}OH$ radicals, which can transform these molecules into carbon dioxide and water [2, 3, 11–13]. Photocatalysis is an environmentally friendly, mild condition, and energy-conservative process with no secondary pollution production [2, 3, 11–13].

ZnO, an n-type semiconductor of group II–VI, is an excellent photocatalyst used for degrading azo organic dyes because it is environmentally friendly, nontoxic, and inexpensive, and has high electron mobility [1, 14–18]. Nevertheless, ZnO with an E_g of 3.37 eV is limited by its practical photocatalytic application in only the UV range, high recombination rate of photo-excited electrons/photo-induced holes, and photocorrosion resistance [14–16, 19–22]. To develop ZnO photocatalyst, it is coupled with other semiconductors [11, 16, 21]. Surface defects [12, 19], metal dopants [14, 15, 20, 23–25], and anion dopants [26, 27] have been investigated in recent years. ZnO coupled with noble metal is the effective way to enhance UV light-driven photocatalytic performance because the loaded noble metallic nanoparticles can play the role in accepting photo-excited electrons from conduction band (CB) of ZnO by creating localized surface plasmon resonance (LSPR) effect, suppressing the rate of carrier recombination and enhancing photocatalytic reaction rate [14, 23, 24, 28, 29]. For examples, Ashkarran reported that he succeeded in preparing Ag/ZnO nanostructure by two times combination of simple arc discharge in liquid and the sample showed enhanced photodegradation of rhodamine B (Rh B), methyl orange (MO) and methylene blue (MB) under visible light irradiation because of the noble Ag as electron trap inside [14]. Zhu et al. reported that the recombination of photogenerated electrons and holes in ZnO under UV-visible light irradiation was effectively suppressed by the loaded Ag. Ag/ZnO photocatalyst has the photocatalytic activity higher than ZnO and commercial TiO_2 P25 [23].

The present research aims to study the weight content effect of Pt dopant on three-dimensional (3D) flower-like ZnO structure in the photocatalytic degradation of methylene blue (MB) as a toxic dye model under UV light irradiation. The 3D flower-like ZnO structure was synthesized by the precipitation method in a solution containing NaOH as a precipitating reagent, followed by calcination at 600 °C for 2 h. The different weight contents of Pt were loaded on the surface of a 3D flower-like ZnO structure by the photodeposition method. Phase, morphology, oxidation state, and optical properties of Pt/ZnO were studied by different analyzers. The as-prepared 0.5% Pt/ZnO nanocomposites showed excellent UV light-driven photocatalytic degradation of MB under UV light irradiation. Furthermore, the photocatalytic mechanism of 0.5% Pt/ZnO nanocomposites in degrading MB was investigated and discussed in this research.

2. Experiment

To prepare the 3D flower-like ZnO structure by a simple direct precipitation method, 0.045 mole $Zn(NO_3)_2{\cdot}6H_2O$ was dissolved in 200 mL reverse osmosis (RO) water, followed by the addition of 40 mL 3 M NaOH solution as a precipitating reagent. Upon magnetically stirring the solution system for 12 h, the Zn^{2+} solution was transformed into a white precipitate suspension. The white precipitate suspension was filtered, washed, dried, and calcined in a laboratory furnace at 600 °C in ambient atmosphere for 2 h to form a 3D flower-like ZnO structure. Subsequently, different weight contents of $H_2PtCl_6{\cdot}xH_2O$ with 0.5%, 1.0%, and 3.0% Pt were dissolved in 200 mL ethylene glycol, including the subsequent addition of 2.5 g 3D flower-like ZnO powder. The system was irradiated by UV light from a UV lamp for 3 h under magnetically stirring. In the end, the as-prepared Pt/ZnO nanocomposites with 0.5%, 1.0%, and 3.0% Pt by weight were collected, washed, and dried for further characterization.

Phase and purity of the samples were analyzed by a Philips X'Pert MPD X-ray diffractometer (XRD) in the range of $10° - 70°$ and at a scanning rate of $0.02°{\cdot}s^{-1}$. The XRD spectra of ZnO and Pt/ZnO were analyzed using the Xpert HighScore Plus-Rietveld Method. Fourier transform infrared (FTIR) spectra of samples were analyzed on a BRUKER TENSOR 27 Fourier transform infrared (FTIR) spectrometer using KBr as a diluting agent. Raman spectra of samples were analyzed on a HORIBA JOBIN YVON T64000 Raman spectrometer with 50 mW and 514.5 nm wavelength Ar green laser. Morphology and elemental analyses of the as-prepared samples were characterized by a scanning electron microscope (SEM, JEOL JSM IT800) equipped with an Oxford INCA energy dispersive X-ray spectrometer (EDS) operated at 15 kV. Elemental composition and oxidation state of samples were determined by an X-ray photoelectron spectrophotometer (XPS, Kratos X-ray Photoelectron Spectrometer–Axis Ultra DLD) using the monochromated Al Kα (1486.6 eV) radiation and C 1 s of 285.1 eV as a standard. Optical properties of samples were analyzed by a UV-visible diffuse reflectance spectrophotometer (UV-vis DRS, Shimadzu UV-2600) in the wavelength range of $200 - 800$ nm at room temperature using $BaSO_4$ as a standard.

To investigate the photocatalytic performance of the as-prepared sample, 200 mg photocatalyst was suspended in 200 mL of 1×10^{-5} M methylene blue (MB) solution in a photocatalytic dark box and magnetically stirred in the dark for 30 min. Subsequently, the solution system was illuminated by a UV light from three 18 W black light blue fluorescent with a wavelength of 370 nm. During illumination, 5 mL of the MB solution was withdrawn from the solution system every 30 min. The residual photocatalyst containing in MB solution was removed by being centrifuged at 4500 rpm and analyzed for the absorption of residual content of MB at λ_{max} of 664 nm by a PerkinElmer Lambda 25 UV/Vis Spectrophotometer. The photocatalytic efficiency was calculated by the below equation.

$$\text{Photocatalytic efficiency}(\%) = \frac{C_0 - C_t}{C_0} \times 100 \quad (1)$$

where C_0 and C_t are the MB concentrations before ($t = 0$) and after ($t = t$) photocatalytic reaction under UV light irradiation. The MB content after photocatalytic reaction over 0.5% Pt/ZnO was analyzed by a 2690 LCT Micromass electrospray ionization (ESI) mass spectrometer in a positive ion mode to determine the final agents left in the photocatalytic solution system.

3. Results and discussion

X-ray diffraction (XRD) pattern of pure ZnO sample (Fig. 1) synthesized by the precipitation method using NaOH as a precipitating reagent, followed by 600 °C calcination in air for 2 h. It was indexed to the pure phase of hexagonal ZnO structure (JCPDS No. 00-036-1451 [30]). Other diffraction peaks of impurities were not detected in the XRD pattern. For the XRD patterns of heterojunction 0.5% and 1.0% Pt/ZnO nanocomposites (Fig. 1), they show diffraction patterns similar to that of the hexagonal ZnO structure without the loaded Pt. The XRD pattern of 3.0% Pt/ZnO nanocomposites (Fig. 1) contains an additional diffraction peak at 2θ of 39.89°, which can be indexed to the (111) diffraction plane of face-centered cubic (FCC) metallic Pt phase (JCPDS No. 00–004–0802 [30]). The particle size (D) of ZnO and Pt was calculated using the Scherrer equation below.

$$D = \frac{K\lambda}{\beta \cos\theta} \tag{2}$$

where K is the shape factor (0.89), λ is the Cu Kα (1.54056 Å) line, and β is the full width at half maximum (FWHM) in radian [31–34]. Moreover, the crystallite size and microstrain of ZnO were calculatedd by the Williamson-Hall equation as follows.

$$\beta \cos\theta = \frac{k\lambda}{D} + 4\varepsilon \sin\theta \tag{3}$$

where ε is the lattice microstrain. Fig. 2 shows the linear plotted graphs of $4\sin\theta$ against $\beta\cos\theta$ for the as-prepared ZnO and Pt/ZnO nanocomposites [32, 35]. The crystallite size of as-prepared ZnO and Pt/ZnO nanocomposites was estimated from the y-intercept, while the strain of as-prepared ZnO and Pt/ZnO nanocomposites was estimated from the slope. The particle size and microstrain of the samples were calculated and summarized in Table 1.

Fourier-transform infrared (FTIR) spectrum of pure ZnO sample (Fig. 3 (a)) shows a sharp FTIR peak at 432 cm^{-1}, which is related to the stretching vibration of Zn–O [2, 12, 15, 18, 25]. For the FTIR spectra of Pt/ZnO nanocomposites (Fig. 3 (a)), the stretching vibration of Zn–O was slightly shifted to 435 cm^{-1} due to the strong

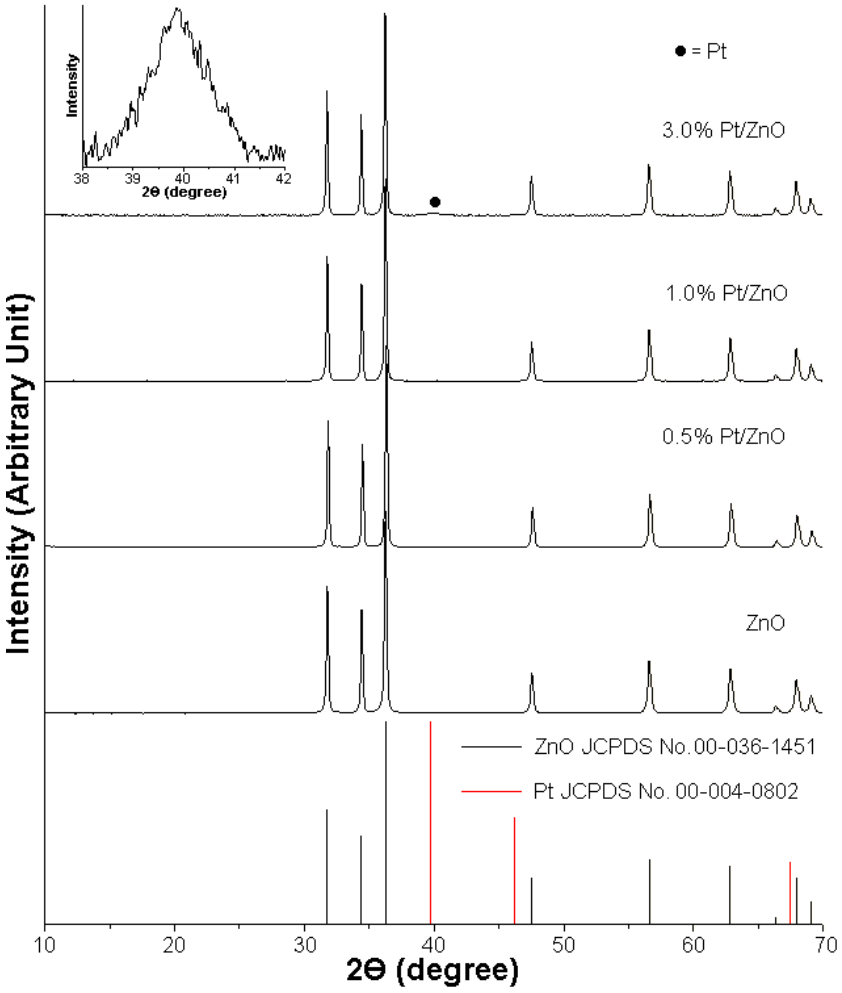

Figure 1. XRD patterns of as-prepared 0.0%, 0.5%, 1.0% and 3.0% Pt/ZnO samples.

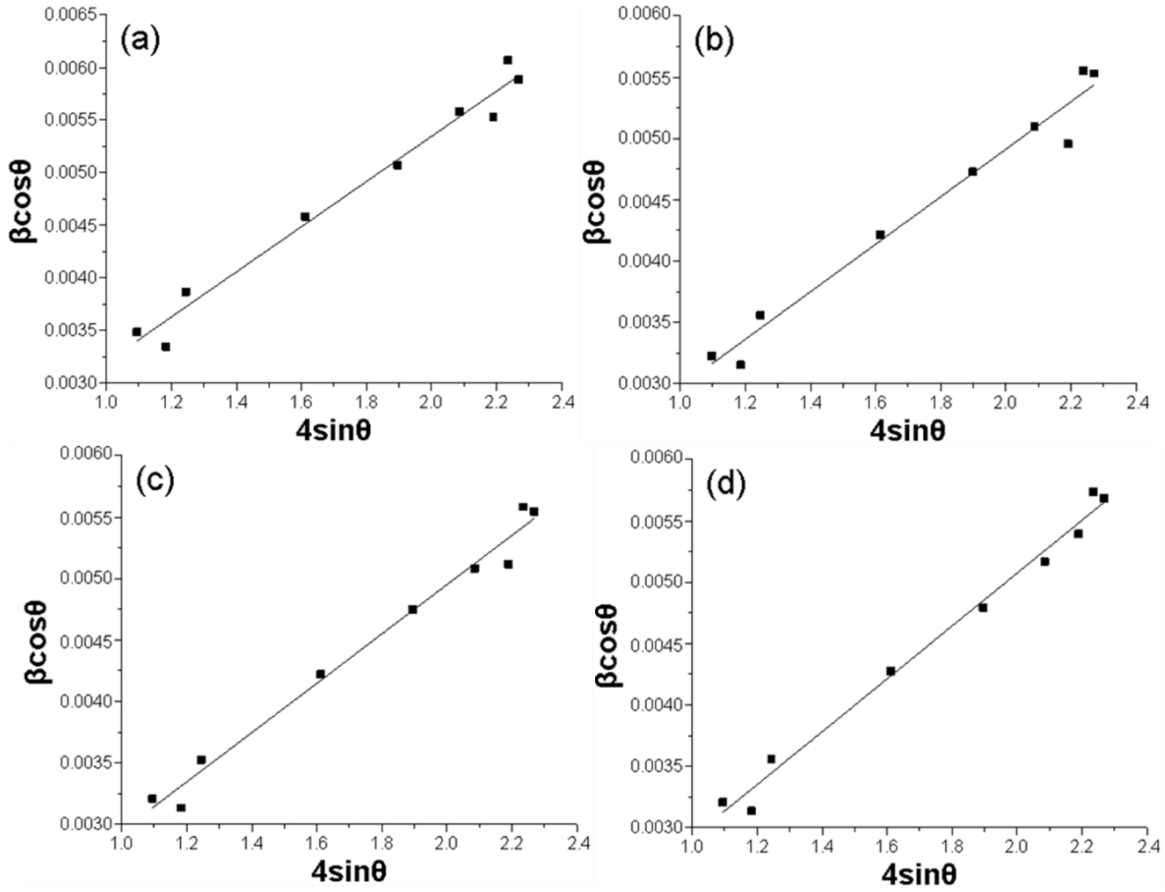

Figure 2. Linear plots of $4\sin\theta$ and $\beta\cos\theta$ of as-prepared (a) ZnO, (b) 0.5% Pt/ZnO, (c) 1.0% Pt/ZnO and (d) 3.0% Pt/ZnO.

interaction of metallic Pt nanoparticles and hexagonal wurtzite ZnO sample. The FTIR spectra of ZnO and heterojunction Pt/ZnO nanocomposites show the broad band at $3200-3650\ cm^{-1}$, which is related to the O–H stretching of adsorbed water on the sample surface [2, 3, 12, 15, 18, 25]. Raman spectrum of pure ZnO sample (Fig. 3 (b)) shows a dominant Raman peak at $436\ cm^{-1}$, which was assigned to the phonon $E_2(H)$ mode of characteristic hexagonal ZnO structure [2, 18, 25, 36]. The intensity of the phonon $E_2(H)$ mode was decreased and broadened when the ZnO sample was loaded with Pt nanoparticles due to the Localized Surface Plasmon Resonance (LSPR) effect of metallic Pt nanoparticles [36–38]. The LSPR is defined as the collective oscillation of conduction electrons near the surface of noble metal illuminated by photonic light, leading to the existence of a localized electromagnetic field with distinct optical properties. The $E_2(H) - E_2(L)$ and A_{1T} modes of the hexagonal ZnO structure were detected at 332 and 379 cm^{-1} [2, 18, 25, 36]. The $E_1(L)$ mode of hexagonal ZnO structure is related to the intrinsic defects such as zinc interstitial (Zn_i) and oxygen vacancy (V_O) at a wavenumber of $583\ cm^{-1}$ [2, 18, 25, 36]. The loaded Pt nanoparticles have the benefit of better photocatalytic activity of ZnO sample [12, 25, 36, 39].

The oxidation state and composition of heterostructure 0.5% Pt/ZnO nanocomposites were analyzed by X-ray photoelectron spectroscopy (XPS) at $0-1200$ eV using C 1s as a standard. Fig. 4 (a) shows the full survey XPS spectrum of heterostructure 0.5% Pt/ZnO nanocomposites. It presents only binding energies of Pt, Zn and O containing in heterostructure 0.5% Pt/ZnO nanocomposites. The heterostructure 0.5% Pt/ZnO nanocomposites are ZnO phase doped

Table 1. Particle size and microstrain of the samples.

Sample	ZnO			Pt
	Scherrer particle size (nm)	W-H particle size (nm)	Microstrain	Scherrer particle size (nm)
ZnO	32.77 ± 7.18	136.616	2.14	-
0.5% Pt/ZnO	27.23 ± 8.13	139.243	1.94	-
1.0% Pt/ZnO	27.22 ± 8.41	154.172	2.01	-
3.0% Pt/ZnO	26.56 ± 8.75	188.593	2.15	7.06

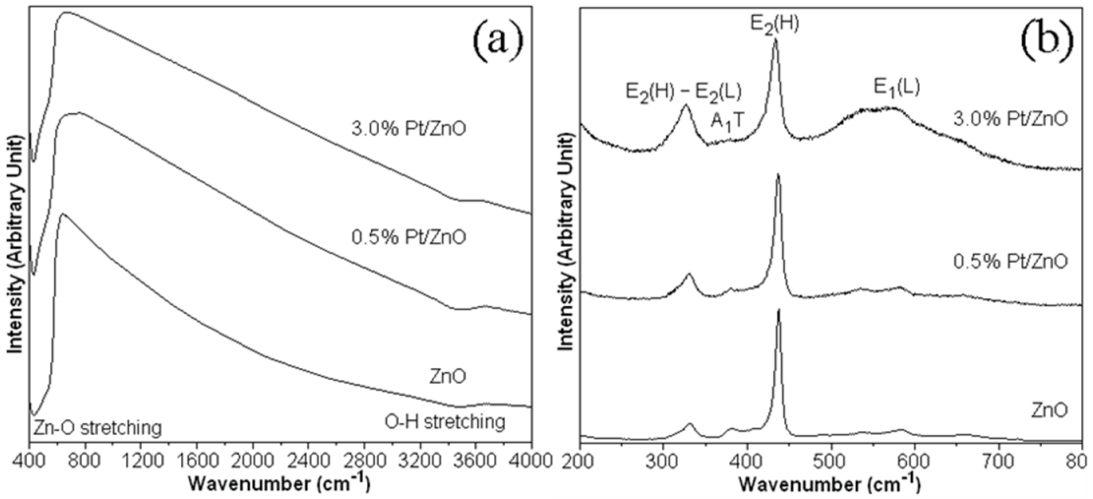

Figure 3. (a) FTIR and (b) Raman spectra of ZnO, 0.5% Pt/ZnO and 3.0% Pt/ZnO samples.

with Pt nanoparticles. Fig. 4 (b) shows high resolution binding energy of Pt 4f core level of heterostructure 0.5% Pt/ZnO nanocomposites. The major high resolution binding energy peaks of Pt $4f_{5/2}$ and Pt $4f_{7/2}$ of metallic Pt^0 containing in heterostructure 0.5% Pt/ZnO nanocomposites were detected at 74.81 eV and 71.47 eV [36, 40–43]. The minor binding energies of Pt 4f at 75.62/72.29, 76.38/73.08 and 77.23/73.95 eV were assigned to the spin orbitals of $Pt4f_{5/2}$/$Pt4f_{7/2}$ for Pt^{2+}/Pt^{4+} because the metallic Pt^0 nanoparticles were oxidized to $Pt(OH)_2$, PtO and PtO_2 [41–43]. The binding energy peaks of Pt $4f_{5/2}$ and Pt $4f_{7/2}$ of metallic Pt^0 in heterostructure 0.5% Pt/ZnO nanocomposites were slightly shifted to the higher values because of the spontaneous electron transfer from Pt nanoparticles to ad-

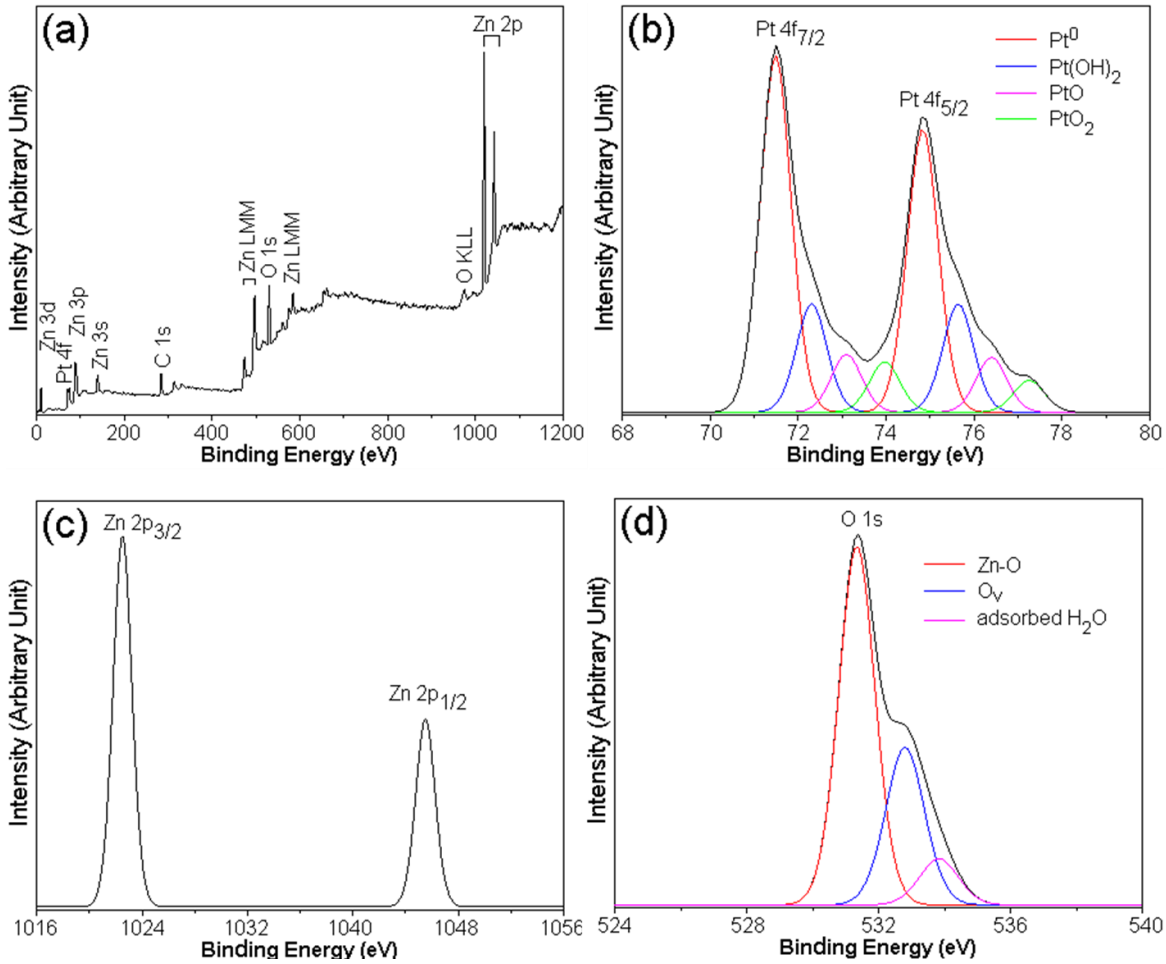

Figure 4. (a) Full XPS survey spectrum and high-resolution spectra of (b) Pt 4f, (c) Zn 2p and (d) O 1s core levels of 0.5% Pt/ZnO nanocomposites.

sorbed oxygen resulting from the difference in Fermi energy of Pt and adsorbed oxygen [44, 45]. The high resolution XPS spectrum of Zn 2p core level (Fig 4 (c)) shows two symmetric binging energy peaks located at 1022.53 eV of Zn $2p_{3/2}$ and 1045.60 eV of Zn $2p_{1/2}$ with energy difference of 23.07 eV. Thus, the oxidation state of Zn species in heterostructure 0.5% Pt/ZnO nanocomposites was 2+ [15, 20, 23, 25]. The asymmetric high resolution XPS spectrum of O 1s of heterostructure 0.5% Pt/ZnO nanocomposites (Fig. 4 (d)) was deconvoluted through the Gaussian fitting model. They were attributed to the Zn–O bond (531.34 eV), Ov (532.83 eV) and adsorbed H_2O on surface of heterostructure 0.5% Pt/ZnO nanocomposites (533.86 eV) [14, 15, 20, 23, 25, 40].

Scanning electron microscopic (SEM) image of as-prepared pure ZnO sample (Fig. 5 (a) and (b)) clearly shows uniform three-dimensional (3D) flower-like ZnO structure with a size of $2-6\ \mu$m. Each 3D flower-like ZnO structure was built up from several hundred nanoplate petals that grew from a single center of the 3D flower-like ZnO structure. The ZnO nanoplates with smooth surfaces have a $80-100$ nm diameter and are $200-1000$ nm long. The SEM images of heterostructure 0.5% and 3.0% Pt/ZnO nanocomposites (Fig. 5 (c–f)) present uniform 3D flower-like ZnO structure with the average size of $2-5\ \mu$m. The SEM images of heterostructure 0.5% and 3.0% Pt/ZnO nanocomposites at

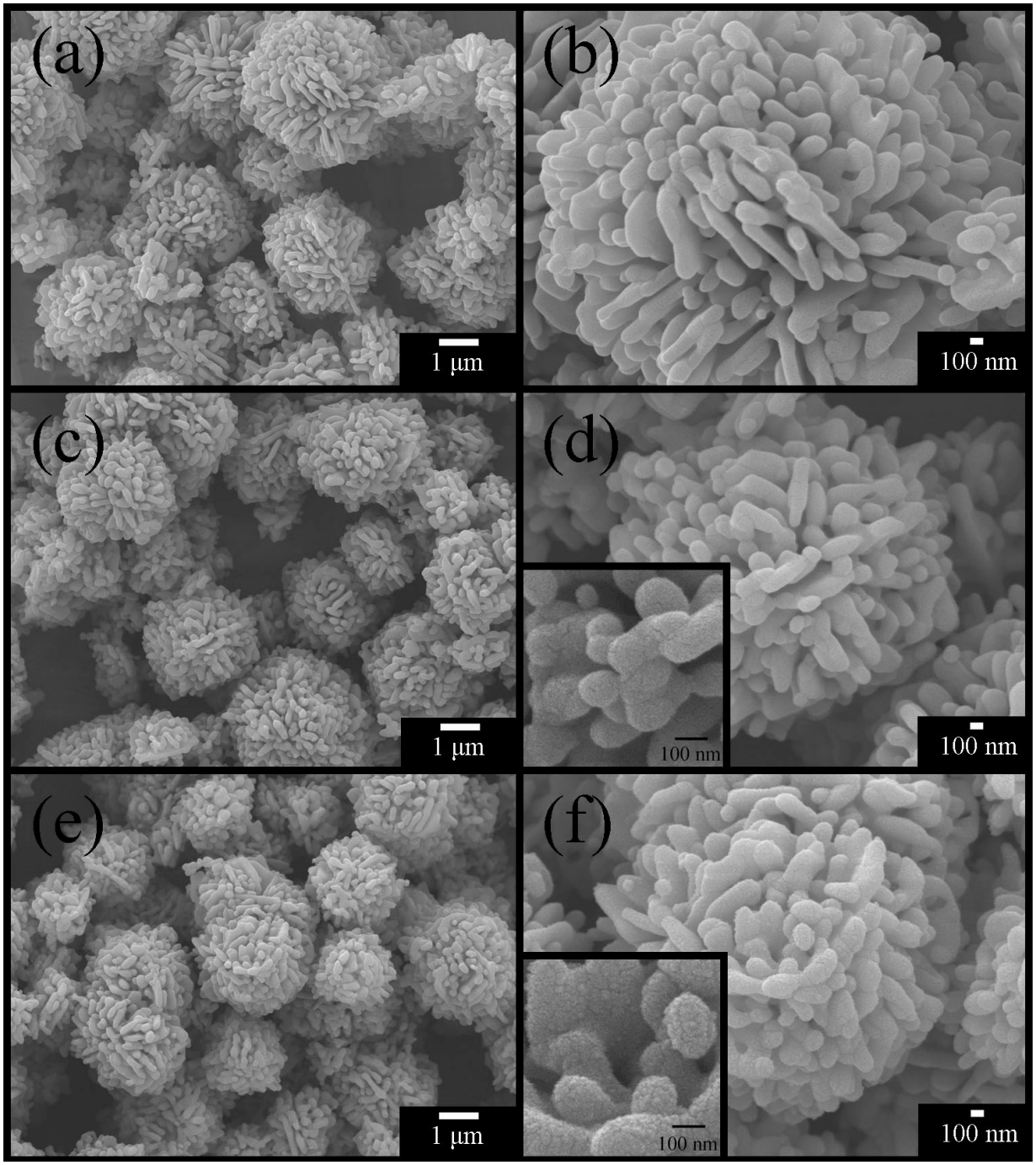

Figure 5. SEM images with high and low magnification of as-prepared (a, b) ZnO, (c, d) 0.5% Pt/ZnO and (e, f) 3.0% Pt/ZnO samples.

high magnification show that the nanoplate petals are rough surface. They can be seen that Pt nanoparticles decorated on top of nanoplate petals of 3D flower-like ZnO structure. These results certified the formation of heterojunction of Pt nanoparticles–nanoplate petals of the 3D flower-like ZnO structure. The elemental constituents of heterostructure 0.5% Pt/ZnO nanocomposites were analyzed by energy dispersive X-ray spectroscopy (EDS) as the results shown in Fig. 6. The analysis certified the presence of Pt (red), Zn (green) and O (yellow) constituents containing in the nanocomposites. The weight percent of Pt, Zn and O in 0.5% Pt/ZnO were calculated and summarized in Table 2. The weight percent of Pt is very close to 0.5%. The metallic Pt nanoparticles were well dispersed on the surface of 3D flower-like ZnO structure. These results indicated the successful synthesis of 3D flower-like ZnO structure loaded with metallic Pt nanoparticles on the top by photodeposition method.

The optical absorbance of ZnO and Pt/ZnO samples (Fig. 7 (a)) was analyzed by UV-vis diffuse reflectance spectroscopy at room temperature using $BaSO_4$ as a reference in a wavelength range of $200-800$ nm. The UV-vis DRS spectrum of 3D flower-like ZnO structure shows the high UV absorption with the absorption edge of 395 nm due to the electronic transition of hexagonal ZnO phase. The 3D flower-like ZnO structure is active only in the UV region [46–48]. When Pt nanoparticles were loaded on the 3D ZnO flowers, the UV-vis DRS spectra of Pt/ZnO nanocomposites in the visible region of $400-700$ nm were strengthened due to the surface plasmon resonance (SPR) effect of Pt nanoparticles [13, 14, 23, 46]. The absorption edge of 3% Pt/ZnO nanocomposites was slightly shifted to 391 nm. The energy gap (E_g) of ZnO and Pt/ZnO samples were calculated by the below Tauc relation.

$$(\alpha h\nu)^2 = A(h\nu - E_g) \tag{4}$$

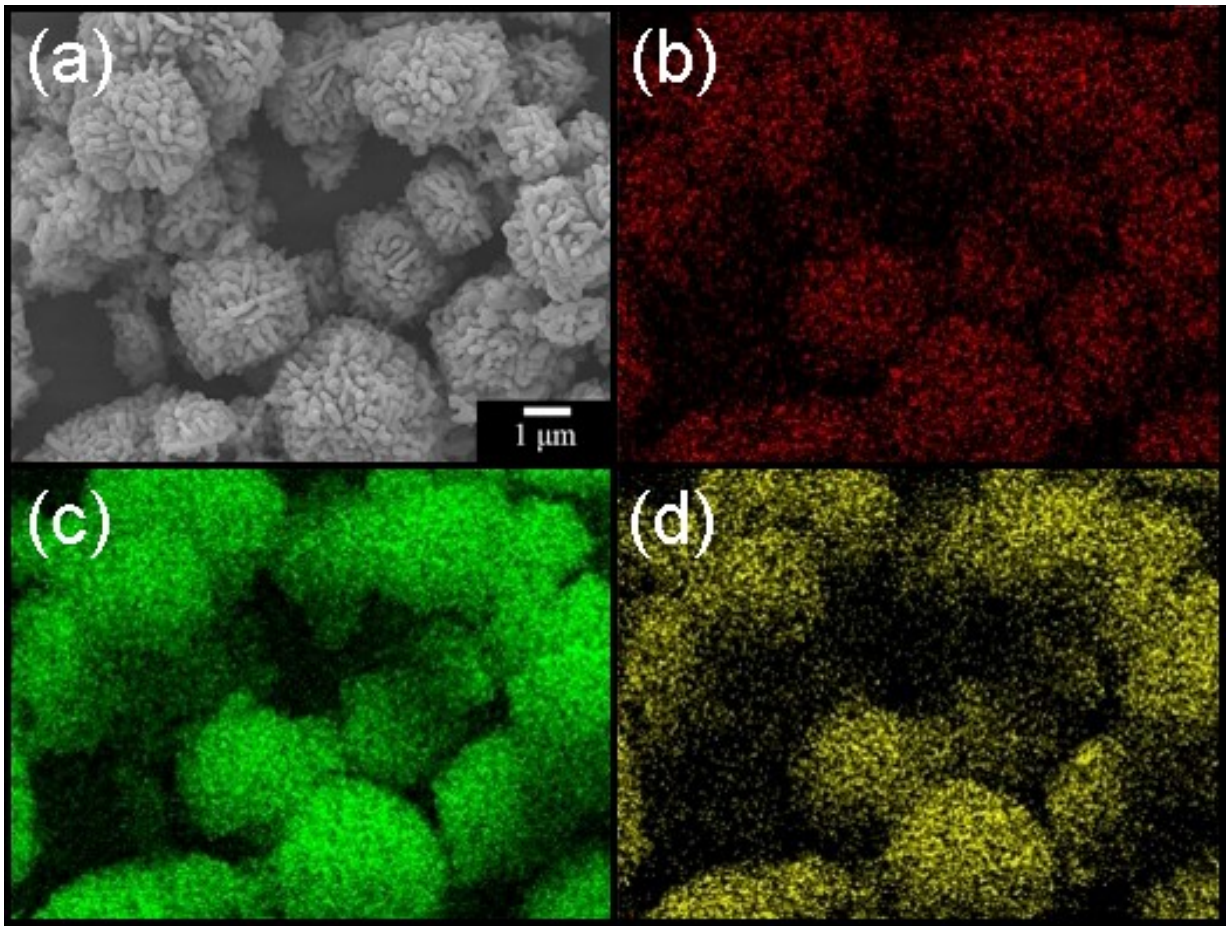

Figure 6. (a) SEM image and EDS maps of (b) Pt, (c) Zn and (d) O containing in 0.5% Pt/ZnO nanocomposites prepared by photoreduction deposition method.

Table 2. Weight percent of Pt, Zn and O containing in 0.5% Pt/ZnO nanocomposites.

Elements	Weight percent (%)
Pt	0.43
Zn	83.45
O	16.12

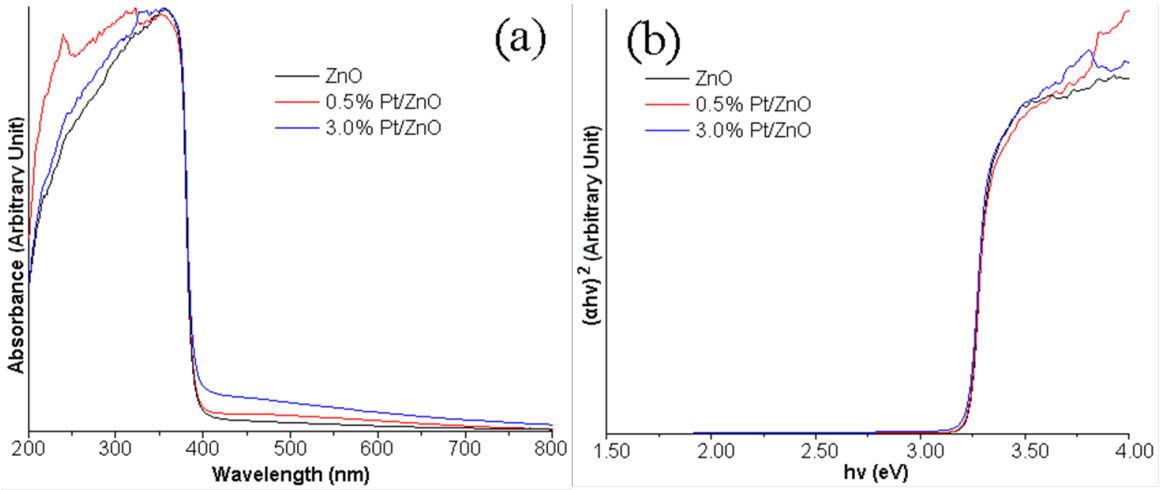

Figure 7. (a) Photonic absorbance and (b) Tauc plots of as-prepared 0.0%, 0.5%, and 3.0% Pt/ZnO samples.

where α is the coefficient of absorbance, A is a constant and $h\nu$ is the photon energy [52–55]. Fig. 7 (b) shows the plot of $(\alpha h\nu)^2$ versus $h\nu$ of ZnO and Pt/ZnO samples. The E_g of ZnO and Pt/ZnO were determined by extrapolating the linear part of the plot of $(\alpha h\nu)^2$ as a function of $h\nu$ to intercept the $h\nu$ axis at zero absorbance. The E_g was decreased from 3.24 eV of ZnO to 3.21 eV of 3% Pt/ZnO nanocomposites caused by the synergetic interaction of Pt nanoparticles and 3D flower-like ZnO structure.

The cationic MB dye was monitored for photocatalytic activity of pure ZnO and Pt/ZnO samples under UV light irradiation. Fig. 8 shows the UV–vis absorbance of MB solution over pure ZnO and 0.5% Pt/ZnO samples for different lengths of UV illumination. They were found that the UV–vis absorbance of MB at 664 nm over heterostructure 0.5% Pt/ZnO nanocomposites were decreased faster than that over pure ZnO sample without the loaded Pt nanoparticles. The results indicated that the loaded Pt played the role in enhancing the photocatalytic performance of ZnO under UV light irradiation.

Fig. 9 (a) shows UV-light-driven photocatalytic performance of the as-prepared 0.0%, 0.5%, 1.0% and 3.0% Pt/ZnO samples. In this research, UV-light-driven photocatalytic efficiencies of heterojunction Pt/ZnO nanocomposites were higher than that of pure ZnO sample. The Pt nanoparticles can play the role in enhancing the photocatalysis of ZnO under UV light irradiation [14, 23, 56, 57]. The photodegradation efficiencies were 37.76%, 97.37%, 69.84% and 55.40% photocatalyzed by 0.0%, 0.5%, 1.0% and 3.0% Pt/ZnO samples, respectively. The UV-light-driven photocatalytic efficiency of heterojunction 0.5% Pt/ZnO nanocomposites was the highest. Pt nanoparticles acted as a conductor for the photo-excited electrons in CB of ZnO. Thus, the recombination of photo-excited electrons–photo-induced holes of ZnO was inhibited and the photocatalytic reaction rate was enhanced [8, 17, 32]. The pseudo-first-order reaction rate constants for photodegradation of MB over the as-prepared ZnO and Pt/ZnO samples under UV light irradiation were expressed by the following.

$$\ln(C_0/C_t) = kt \tag{5}$$

where C_0 and C_t are the concentrations of MB in the dark ($t = 0$) and after UV irradiation for a period of time $t = t$ [56, 58, 59]. The pseudo-first-order plots (Fig. 9 (b)) fol-

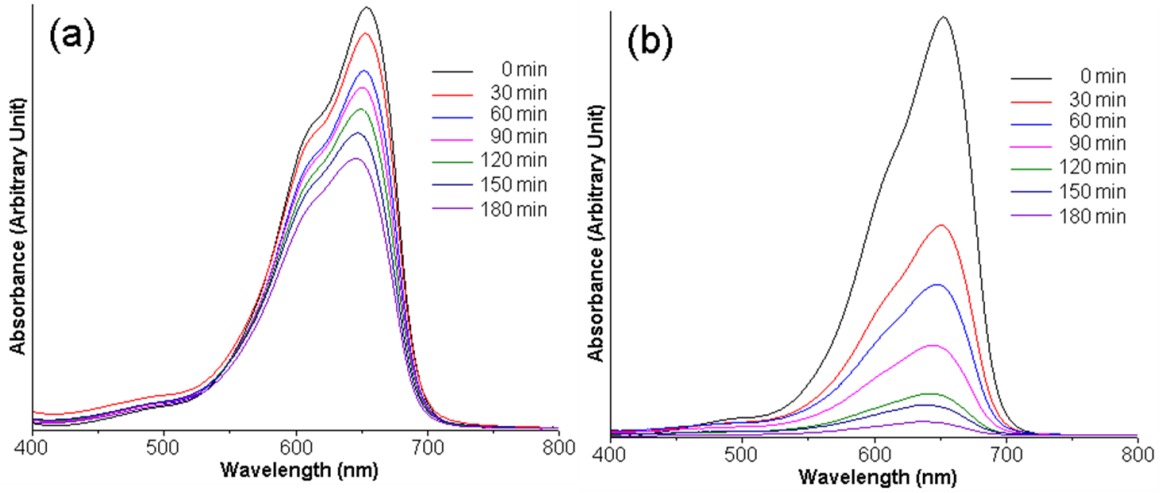

Figure 8. UV–vis absorbance of MB photocatalyzed by pure ZnO and 0.5% Pt/ZnO samples for different lengths of illumination time.

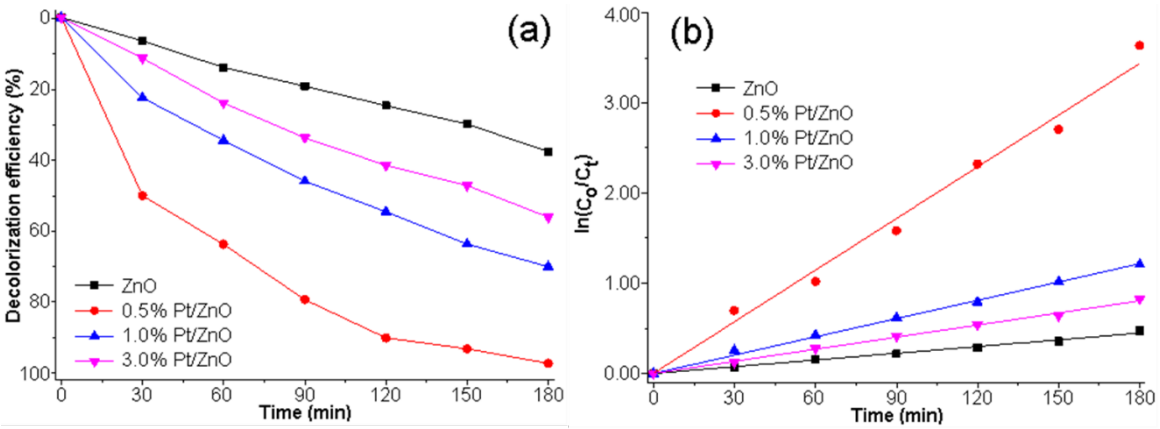

Figure 9. (a) UV-light-driven photocatalytic performance and (b) pseudo-first-order kinetics of as-prepared 0.0%, 0.5%, 1.0% and 3.0% Pt/ZnO nanocomposites in degrading MB.

lowed the linear lines with $R^2 \rightarrow 1$ for all the photocatalysts [1, 2, 14, 15, 18, 60]. The kinetic rate constants were 2.42×10^{-3}, 0.0192, 6.74×10^{-3} and 4.57×10^{-3} min^{-1} for MB degradation photocatalyzed by 0.0%, 0.5%, 1.0% and 3.0% Pt/ZnO samples, respectively. The degradation of MB photocatalyzed by heterojunction 0.5% Pt/ZnO nanocomposites was the highest. The photocatalytic efficiencies of the present and previous works were compared in Table 3. Clearly, the 0.5% Pt/ZnO nanocomposites show the photocatalytic performance higher than the pure ZnO sample and other metal or metal oxide-doped ZnO samples due to the formation of a heterojunction between the noble metal nanoparticles and the semiconductor photocatalyst [17, 18, 46–51].

The MB solutions before and after being photocatalyzed by heterojunction 0.5% Pt/ZnO nanocomposites for different lengths of time were analyzed by mass spectroscopy in a positive mode (Fig. 10). The mass spectrum of pure MB ($C_{16}H_{18}N_3S^+Cl^-$) before photocatalytic reaction shows the mass to charge (m/z) ratio of 284 [7, 61–63]. When the photocatalytic reaction was proceeding, hydroxyl radicals and reactive oxygen species (ROS) played the role in attacking MB in a multi-step pathway with the subsequent formation of thionine acetate, azure A and B products, including single and double ring structured products. hydrazinecarbothioamide, N-(phenylmethyl)-2-(phenylmethylene) ($C_{15}H_{15}N_3S^+$, m/z = 270), 2-chlorobenzaldehyde N-phenylthiosemicarbazone ($C_{14}H_{12}N_3S^+$, m/z = 256) and 3-(5-Phenyl-1,3,4-thiadiazol-2-yl)pyridine ($C_{13}H_9N_3S$, m/z = 242) formed and were transformed into small alicyclic organic compounds and followed with open ring into aliphatic compounds [7, 61–64]. New m/z = 148, 141, 133, 131 and 122 were detected with the final formation of CO_2, H_2O, Cl^-,

Table 3. Comparison for photocatalytic efficiencies of the present and previous works.

Photocatalysts	Dyes	Light irradiation	Photocatalytic performance	References
Cu_2O/ZnO composites	MO	Visible light	98% within 240 min	[17]
2D ZnO nanoplates			97.54% within 240 min	
ZnO multi-layered nanorod microflowers	MB	UV light	77.82% within 240 min	[18]
ZnO pyramid tip microflowers			89.10% within 240 min	
Ag/ZnO nanocomposites	MB	Sun light	98.95% within 210 min	[46]
ZnO nanoparticles	MB	UV light	100% within 210 min	[47]
	MO		82.78% within 210 min	
Cu-doped ZnO nanoparticles	MB	UV light	85% within 210 min	[48]
		Visible light	90% within 210 min	
Co-doped ZnO thin films	MB	UV light	91.3% within 210 min	[49]
In-doped ZnO thin films			85% within 210 min	
Mg-doped ZnO thin films	MB	UV light	97% within 330 min	[50]
Mn-doped ZnO nanoparticles	Orange II	Visible light	~ 75% within 240 min	[51]
0.5% Pt/ZnO nanocomposites	MB	UV light	97.37% within 180 min	This work

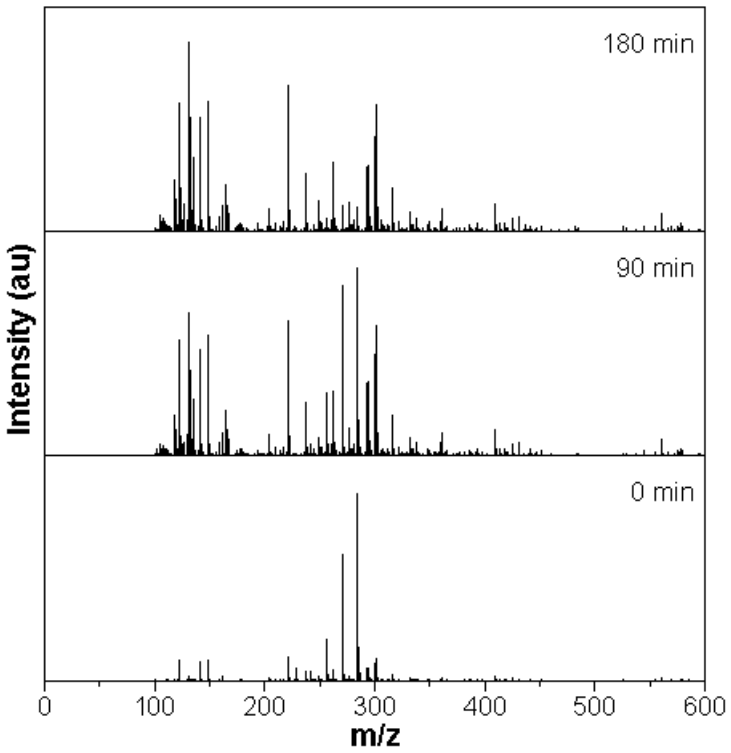

Figure 10. Mass spectroscopy of MB over 0.5% Pt/ZnO nanocomposites under UV light irradiation at the time of 0 min (in the dark) and at the end of 90 min and 180 min photocatalysis.

SO_4^{2-} and NO_3^- at the conclusion of 180 min.

Fig 11a shows the photocatalytic efficiencies for MB degradation of the cyclic experiment of 0.5% Pt/ZnO nanocomposites illuminated by UV light. At the end of each photocatalytic cycle, the re-used 0.5% Pt/ZnO nanocomposites were collected by filtration, washed with 95% ethanol and dried for the next photocatalytic cycle. The photocatalytic efficiency was little reduced to 94.35% at the end of cycle five. The results indicated that Pt/ZnO nanocomposites are excellently stable and recyclable in practical application.

Isopropanol (IPA), p-benzoquinone (BQ) and disodium ethylene diamine tetraacetate (EDTA-2Na) were also added in photocatalytic solutions in order to trap hydroxyl radical ($^{\bullet}OH$), superoxide radical ($^{\bullet}O_2^-$) and hole (h^+) during MB degradation photocatalyzed by the as-prepared 0.5% Pt/ZnO nanocomposites [60, 65–68]. Fig. 11 (b) shows the photocatalytic efficiencies for MB degradation with and without different scavengers photocatalyzed by 0.5% Pt/ZnO nanocomposites under UV light irradiation. In this research, the photocatalytic efficiencies were much suppressed by BQ and EDTA-2Na and were reduced to 10.98% and 32.79% for MB degradation under UV light irradiation within 180 min. The photodegradation for MB with IPA adding over 0.5% Pd/ZnO nanocomposites was slightly decreased to 82.13% within 180 min under UV light irradiation. Thus, $^{\bullet}OH$ was not involved in photocatalysis of MB by 0.5% Pt/ZnO nanocomposites under UV light irradiation. In conclusion, $^{\bullet}O_2^-$ and h^+ were the main active species used for dye degradation over 0.5% Pt/ZnO nanocomposites under UV light irradiation [14, 23, 56, 67].

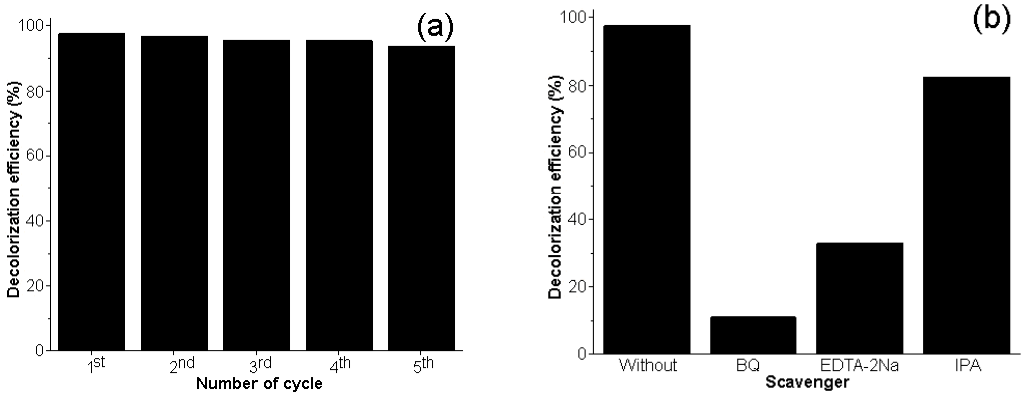

Figure 11. (a) Photocatalytic performance of re-used 0.5% Pt/ZnO nanocomposites in degrading MB for five cycles. (b) Effect of different trapping agent during photocatalysis of 0.5% Pt/ZnO nanocomposites.

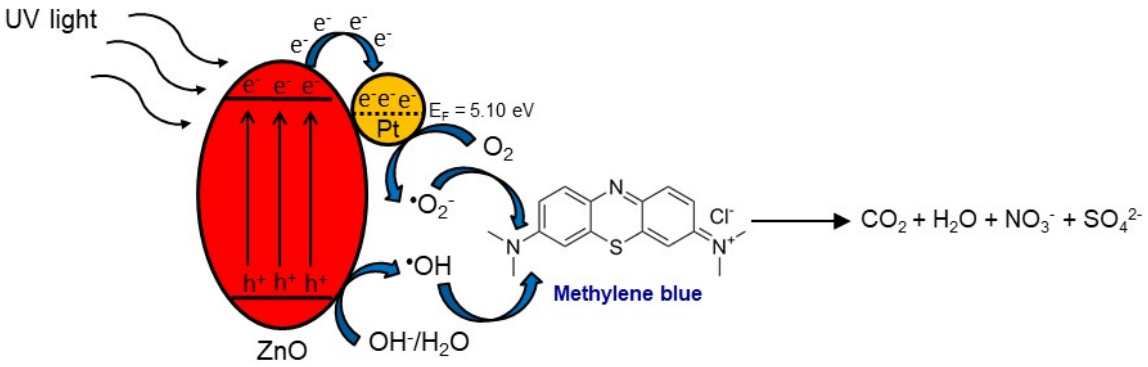

Figure 12. A possible UV-light-driven photocatalytic mechanism of as-prepared Pt/ZnO nanocomposites in degrading MB.

Fig. 12 shows a possible UV-light-driven photocatalytic performance for MB degradation over as-prepared Pt/ZnO nanocomposites. Under UV light irradiation, electrons were excited from valence band (VB) to conduction band (CB) of ZnO with the induction of holes in the valence band (VB) [1, 14, 23, 56, 67]. To prevent the recombination of electrons–holes, photo-excited electrons in CB of ZnO diffuse to the Pt nanoparticles acted as electron conductor due to the lower Fermi level of Pt nanoparticles [14, 23, 56, 67]. Subsequently, the adsorbed O_2 and adsorbed OH^-/H_2O combined with the photo-excited electrons and photo-induced holes to form $^{\bullet}O_2^-$ and $^{\bullet}OH$ radicals which played the role in degrading MB and transformed the dye into CO_2, H_2O and small inorganic ions [14, 23, 56, 67].

4. Conclusion

Heterojunction Pt/ZnO nanocomposites were successfully synthesized by a photoreduction deposition for MB degradation under UV light irradiation. In this research, weight content of the loaded Pt on 3D flower-like ZnO structure was the key parameter for UV light-driven photocatalytic degradation of MB. The heterojunction 0.5% Pt/ZnO nanocomposites have the highest UV light-driven photocatalytic activity and $^{\bullet}O_2^-$ and h^+ were the main active radicals. Furthermore, the heterojunction 0.5% Pt/ZnO nanocomposites were excellently stable and recyclable in practical photocatalytic application.

Acknowledgement
This research was supported by the National Science, Research and Innovation Fund (NSRF), Thailand, and Prince of Songkla University (grant no SCI6801030S).

Authors contributions
Authors have contributed equally in preparing and writing the manuscript.

Availability of data and materials
The data that support the findings of this study are available from the corresponding author, upon reasonable request.

Conflict of interests
The author declare that they have no known competing financial interests or personal relationships that could have appeared to influence the work reported in this paper.

References

[1] R. A. Alshgari, Z. A. Ujjan, A. A. Shah, M. A. Bhatti, A. Tahira, N. M. Shaikh, S. Kumar, M. H. Ibupoto, A. Elhawary, A. Nafady, B. Vigolo, and Z. H. Ibhupoto. *Molecules*, **27**(2022):8726. DOI: https://doi.org/10.3390/molecules27248726.

[2] A. Phuruangrat, B. Kuntalue, S. Thongtem, and T. Thongtem. *Optik*, **226**(2021):165949, . DOI: https://doi.org/10.1016/j.ijleo.2020.165949.

[3] R. Wang, Z. Jiang, L. Xu, and C. Liu. *J. Mater. Sci.: Mater. Electron.*, **32**(2021):6931, . DOI: https://doi.org/10.1007/s10854-021-05399-3.

[4] S. Zhong, C. Lv, M. Shen, L. Wu, and C. Li. *J. Mater. Sci.: Mater. Electron.*, **30**(2019):4152. DOI: https://doi.org/10.1007/s10854-019-00707-4.

[5] I. Khan, K. Saeed, I. Zekker, B. Zhang, A. H. Hendi, A. Ahmad, S. Ahmad, N. Zada, H. Ahmad, L. A. Shah, T. Shah, and I. Khan. *Water*, **14**(2022):242. DOI: https://doi.org/10.3390/w14020242.

[6] M. I. Din, R. Khalid, J. Najeeb, and Z. Hussain. *J. Clean. Prod.*, **298**(2021):126567. DOI: https://doi.org/10.1016/j.jclepro.2021.126567.

[7] O. M. A. Halim, N. H. Mustapha, S. N. M. Fudzi, R. Azhar, N. I. N. Zanal, N. F. Nazua, A. H. Nordin, M. S. M. Azami, M. A. M. Ishak, W. I. N. W. Ismail, , and Z. Ahmad. *Results Surf. Interfaces*, **18**(2025): 100408. DOI: https://doi.org/10.1016/j.rsurfi.2024.100408.

[8] S. A. Mirsalari, A. Nezamzadeh-Ejhieh, and A. R. Massah. *Environ. Sci. Pollut. Res.*, **29**(2022):33013. DOI: https://doi.org/10.1007/s11356-021-17569-1.

[9] M. Farsi and A. Nezamzadeh-Ejhieh. *Surf. Interfaces*, **32**(2022): 102148. DOI: https://doi.org/10.1016/j.surfin.2022.102148.

[10] H. Derikvandi, M. Vosough, and A. Nezamzadeh-Ejhieh. *Inter. J. Hydrogen Energy*, **46**(2021):2049, . DOI: https://doi.org/10.1016/j.ijhydene.2020.10.065.

[11] M. Alhaddad and R. M. Mohamed. *Appl. Nanosci.*, **10**(2020):2269. DOI: https://doi.org/10.1007/s13204-020-01359-1.

[12] W. A. Nimpoeno, H. O. Lintang, and L. Yuliati. *IOP Conf. Ser.: Mater. Sci. Eng.*, **833**(2020):012080. DOI: https://doi.org/10.1088/1757-899X/833/1/012080.

[13] L. An, G. Wang, X. Zhou, Y. Wang, F. Gao, and Y. Cheng. *Russ. J. Phys. Chem. A*, **88**(2024)(13). DOI: https://doi.org/10.1134/S003602441413010X.

[14] A. A. Ashkarran. *Appl. Phys. A*, **107**(2012):401.
DOI: https://doi.org/10.1007/s00339-012-6797-6.

[15] D. Laokae, A. Phuruangrat, T. Thongtem, and S. Thongtem. *Russ. J. Inorg. Chem.*, **67**(2022):721.
DOI: https://doi.org/10.1134/S0036023622050114.

[16] J. Liu, Z. Shi, X. Li, J. Yang, and J. Lang. *J. Mater. Sci.: Mater. Electron.*, **30**(2019):13690.
DOI: https://doi.org/10.1007/s10854-019-01746-7.

[17] X. S. Wang, Y. D. Zhang, Q. C. Wang, B. Dong, Y. J. Wang, and W. Feng. *Sci. Eng. Compos. Mater.*, **26**(2019):104, .
DOI: https://doi.org/10.1515/secm-2018-0170.

[18] A. Phuruangrat, S. Thongtem, and T. Thongtem. *Mater. Des.*, **107**(2016):250, .
DOI: https://doi.org/10.1016/j.matdes.2016.06.045.

[19] J. Wang, Y. Xia, Y. Dong, R. Chen, L. Xiang, and S. Komarneni. *Appl. Catal. B*, **192**(2016):8, .
DOI: https://doi.org/10.1016/j.apcatb.2016.03.040.

[20] I. Ahmad, M. S. Akhtar, E. Ahmed, and M. Ahmad. *J. Mater. Sci.: Mater. Electron.*, **31**(2020):1084.
DOI: https://doi.org/10.1007/s10854-019-02620-2.

[21] O. Długosz and M. Banach. *Appl. Nanosci.*, **11**(2021):1707.
DOI: https://doi.org/10.1007/s13204-021-01788-6.

[22] X. Chen, Z. Wu, Z. Gao, and B. C. Ye. *Nanomaterials*, **7**(2017):258.
DOI: https://doi.org/10.3390/nano7090258.

[23] A. Ziashahabi, M. Prato, Z. Dang, R. Poursalehi, and N. Naseri. *Sci. Rep.*, **9**(2019):11839.
DOI: https://doi.org/10.1038/s41598-019-48075-7.

[24] X. Zhu, J. Wang, D. Yang, J. Liu, L. He, M. Tang, W. Feng, and X. Wu. *RSC Adv.*, **11**(2021):27257.
DOI: https://doi.org/10.1039/d1ra05060e.

[25] A. Phuruangrat, P. Sittiangkul, T. Thongtem, and S. Thongtem. *Desalin. Water Treat.*, **280**(2022):338, .
DOI: https://doi.org/10.5004/dwt.2022.29115.

[26] J. Podporska-Carroll, A. Myles, B. Quilty, D. E. McCormack, R. Fagan, S. J. Hinder, D. D. Dionysiou, and S. C. Pillai. *J. Hazard. Mater.*, **324**(2017):39.
DOI: https://doi.org/10.1016/j.jhazmat.2015.12.038.

[27] A. Jiamprasertboon, M. J. Powell, S. C. Dixon, R. Quesada-Cabrera, A. M. Alotaibi, Y. Lu, A. Zhuang, S. Sathasivam, T. Siritanon, I. P. Parkin, and C. J. Carmalt. *J. Mater. Chem. A*, **6**(2018):12682.
DOI: https://doi.org/10.1039/c8ta01420e.

[28] J. Gupta, J. Mohapatra, and D. Bahadur. *Dalton Trans.*, **46**(2017):685.
DOI: https://doi.org/10.1039/C6DT03713E.

[29] H. Derikvandi, M. Vosough, and A. Nezamzadeh-Ejhieh. *Environ. Sci. Pollut. Res.*, **27**(2020):27582, .
DOI: https://doi.org/10.1007/s11356-020-08817-x.

[30] Powder Diffract. File, jcpds internat. centre diffract. data, 12 campus blvd., newtown square, pa 19073–3273. (2004).

[31] A. Yousefi and A. Nezamzadeh-Ejhieh. *Iran. J. Catal.*, **11**(2021):247–259.

[32] M. Rezaei and A. Nezamzadeh-Ejhieha. *Inter. J. Hydrogen Energy*, **45**(2020):24749.
DOI: https://doi.org/10.1016/j.ijhydene.2020.06.258.

[33] A. Norouzi, A. Nezamzadeh-Ejhieh, and R. Fazaeli. *Mater. Sci. Semicond. Process.*, **122**(2021):105495.
DOI: https://doi.org/10.1016/j.mssp.2020.105495.

[34] L. Daneshvar and A. Nezamzadeh-Ejhieh. *Desalin. Water Treat.*, **141**(2019):364.
DOI: https://doi.org/10.5004/dwt.2019.23310.

[35] S. Sharafzadeh, J. Zolgharnein, A. Nezamzadeh–Ejhieh, and S. D. Farahani. *Surf. Interfaces*, **59**(2025):105917, .
DOI: https://doi.org/10.1016/j.surfin.2025.105917.

[36] T. N. T. Oliveira, C. A. Zito, T. M. Perfecto, G. M. Azevedo, and D. P. Volantia. *New J. Chem.*, **44**(2020):15574.
DOI: https://doi.org/10.1039/x0xx00000x.

[37] T. Bora, D. Zoepfl, and J. Dutta. *Sci. Rep.*, **6**(2016):26913.
DOI: https://doi.org/10.1038/srep26913.

[38] S. Y. Sawant, J. Y. Kim, T. H. Han, S. A. Ansari, and M. H. Cho. *New J. Chem.*, **42**(2018):1995.
DOI: https://doi.org/10.1039/c7nj03936k.

[39] K. A. Elsayed, M. Alomari, Q. A. Drmosh, M. Alheshibri, A. A. Baroot, T. S. Kayed, A. A. Manda, and A. L. Al-Alotaibi. *Alex. Eng. J.*, **61**(2022):1449.
DOI: https://doi.org/10.1016/j.aej.2021.06.051.

[40] S. M. Albukhari and A. A. Ismail. *ACS Omega*, **6**(2021):23378.
DOI: https://doi.org/10.1021/acsomega.1c03259.

[41] K. S. Al-Namshah. *Appl. Nanosci.*, **9**(2019):461.
DOI: https://doi.org/10.1007/s13204-018-0900-z.

[42] H. Hagiwara, M. Nagatomo, C. Seto, S. Ida, and T. Ishiahara. *Catalysts*, **3**(2013):614.
DOI: https://doi.org/10.3390/catal3030614.

[43] B. Budner, W. Tokarz, S. Dyjak, A. Czerwiński, B. Bartosewicz, and B. Jankiewicz. *Beilstein J. Nanotechnol.*, **14**(2023):190.
DOI: https://doi.org/10.3762/bjnano.14.19.

[44] T. S. Tofa, F. Ye, K. L. Kunjali, and J. Dutta. *Catalysts*, **9**(2019):819.
DOI: https://doi.org/10.3390/catal9100819.

[45] T. Kiyonag and A. Heima. *MethodsX*, **5**(2018):1484.
DOI: https://doi.org/10.1016/j.mex.2018.11.005.

[46] M. S. A. Galil, M. Al-qubati, S. O. Mohammed, A. Numan, A. A. R. Saeed, and E. A. A. Saif. *Kuwait J. Sci.*, **52**(2025):100356.
DOI: https://doi.org/10.1016/j.kjs.2024.100356.

[47] V. T. T. Nhu, N. D. Dat, L. M. Tam, and N. H. Phuong. *Beilstein J. Nanotechnol.*, **13**(2022):1108.
DOI: https://doi.org/10.3762/bjnano.13.94.

[48] A. Fazil, S. Narayanan, M. S. Begum, G. Manikandan, and M. Yuvashree. *Water Sci. Technol.*, **84**(2021):2958.
DOI: https://doi.org/10.2166/wst.2021.30.

[49] S. B. Ameur, H. BelHadjltaief, B. Duponchel, G. Leroy, M. Amlouk, H. Guermazi, and S. Guermazi. *Heliyon*, **5**(2019):e01912, .
DOI: https://doi.org/10.1016/j.heliyon.2019.e01912.

[50] I. Ameur, B. Boudine, M. Laidoudi, M. Khennoucha, V. Brien, D. Horwat, M. Sebais, and O. Halimi. *Appl. Phys. A*, **127**(2021):331, .
DOI: https://doi.org/10.1007/s00339-021-04486-w.

[51] F. Achouri, S. Corbel, L. Balan, K. Mozet, E. Girot, G. Medjahdid, M. BenSaid, A. Ghrabi, and R. Schneider. *Mater. Des.*, **101**(2016):309.
DOI: https://doi.org/10.1016/j.matdes.2016.04.015.

[52] M. Rezaei, A. A. Ensafi, and E. Heydari-Bafrooei. *Colloids Surf. A*, **708**(2025):135993, .
DOI: https://doi.org/10.1016/j.colsurfa.2024.135993.

[53] M. Rezaei, A. A. Ensafi, and E. Heydari-Bafrooei. *J. Indust. Eng. Chem.*, **146**(2025):589, .
DOI: https://doi.org/10.1016/j.jiec.2024.11.043.

[54] M. Rezaei and A. A. Ensafi. *Mater. Sci. Semicond. Process.*, **188**(2025):109162.
DOI: https://doi.org/10.1016/j.mssp.2024.109162.

[55] S. Ghattavi and A. Nezamzadeh-Ejhieh. *J. Mol. Liq.*, **322**(2021): 114563, .
DOI: https://doi.org/10.1016/j.molliq.2020.114563.

[56] Y. Xia, T. Le, J. Peng, A. V. Ravindra, and L. Xu. *J. Porous Mater.*, **27**(2020):1339.
DOI: https://doi.org/10.1007/s10934-020-00906-z.

[57] S. Shuang, R. Lv, Z. Xie, and Z. Zhang. *Sci. Rep.*, **6**(2016):26670.
DOI: https://doi.org/10.1038/srep26670.

[58] S. Ghattavi and A. Nezamzadeh-Ejhieh. *Desalin. Water Treat.*, **166**(2019):92, .
DOI: https://doi.org/10.5004/dwt.2019.24638.

[59] S. Sharafzadeh, J. Zolgharnein, A. Nezamzadeh–Ejhieh, and S. D. Farahani. *Inter. J. Hydrogen Energy*, **106**(2025):1429, .
DOI: https://doi.org/10.1016/j.ijhydene.2025.02.031.

[60] Y. T. Zhang, D. Y. Wang, X. Luo, K. Lei, L. J. Mao, Y. J. Duan, X. H. Zeng, G. J. Wan, Q. Zhaoc, and Y. Suna. *Dig. J. Nanomater. Bios.*, **19**(2024):571.
DOI: https://doi.org/10.15251/DJNB.2024.192.571.

[61] S. Ghattavi and A. Nezamzadeh-Ejhieh. *Compos. B*, **183**(2020): 107712, .
DOI: https://doi.org/10.1016/j.compositesb.2019.107712.

[62] A. Nezamzadeh-Ejhieha and M. Karimi-Shamsabadi. *Appl. Catal. A*, **77**(2014):83.
DOI: https://doi.org/10.1016/j.apcata.2014.02.031.

[63] P. Jia, H. Tan, K. Liu, and W. Gao. *Mater. Res. Bull.*, **102**(2018): 450.
DOI: https://doi.org/10.1016/j.materresbull.2018.02.018.

[64] T. Shao, Z. Gong, T. Su, W. Hao, and C. Che. *Beilstein J. Org. Chem.*, **13**(2017):817.
DOI: https://doi.org/10.3762/bjoc.13.82.

[65] Q. Qin, L. Zhang, T. Xiao, Y. Y. Zhong, J. Wang, W. L. Liang, Y. H. Wang, S. C. Yanga, and X. D. Zhu. *Dig. J. Nanomater. Bios.*, **19**(2024):549.
DOI: https://doi.org/10.15251/DJNB.2024.192.549.

[66] J. Gao, Y. J. Chen, J. T. Shuai, X. Y. Liu, B. N. Zou, W. Feng, P. Wang, and J. Q. Chen. *Dig. J. Nanomater. Bios.*, **19**(2024):649.
DOI: https://doi.org/10.15251/DJNB.2024.192.649.

[67] P. Hemmatpour and A. Nezamzadeh-Ejhieh. *Chemosphere*, **307**(2022):135925.
DOI: https://doi.org/10.1016/j.chemosphere.2022.135925.

[68] A. Nezamzadeh-Ejhieh and S. Hushmandrad. *Appl. Catal. A*, **388**(2010):149.
DOI: https://doi.org/10.1016/j.apcata.2010.08.042.